Interrelations of atomic structures, electronic structures, electron transport, and magnetic properties across the metal - insulator transition for amorphous V_xSi_{100-x} $(7 \leqslant x \leqslant 74)$ alloys

1997 J. Phys.: Condens. Matter 9 5333

(http://iopscience.iop.org/0953-8984/9/25/004)

J. Phys.: Condens. Matter **9** (1997) 5333–5353. Printed in the UK PII: S0953-8984(97)79353-6

Interrelations of atomic structures, electronic structures, electron transport, and magnetic properties across the metal–insulator transition for amorphous V_xSi_{100-x} ($7 \leqslant x \leqslant 74$) alloys

U Mizutani, T Ishizuka and T Fukunaga

Department of Crystalline Materials Science, Nagoya University, Furo-cho, Chikusa-ku, Nagoya 464-01, Japan

Received 7 November 1996, in final form 14 March 1997

Abstract. The interrelations of the atomic structures, electronic structures, electron transport, and magnetic properties for the amorphous V_xSi_{100-x} alloy system have been studied over a wide composition range, $7 \leqslant x \leqslant 74$, with particular attention paid to their changes across the metal–insulator transition. By analysing the temperature dependence of the conductivity, we concluded that the metal–insulator transition occurs in the composition range $15 < x < 20$. Structural studies revealed that the V atom is substituted for the Si atom in the tetrahedrally bonded Si network in the range where $x < 10$, whereas the local atomic structure resembles that of the VSi_2 intermetallic compound in the range $20 < x < 40$. These two local structures are apparently competing with each other in the critical composition range $10 < x < 20$. Both XPS valence band spectra and electronic specific heat measurements proved that the density of states at the Fermi level is definitely finite even in the insulating regime, i.e., for $x < 15$. Both V Lα and Si Kβ SXS measurements showed that the V 3d states appear just below the Fermi level, and hybridize with the Si 3p states. It is also found that the V atom in the insulating regime possesses a localized magnetic moment, and that the magnetic susceptibility gives rise to a Curie–Weiss-like temperature dependence at low temperatures. Finally, the uniqueness of the electron transport properties for the amorphous V_xSi_{100-x} alloys is emphasized by the ρ–γ diagram, in which the metal–insulator transition is shown to occur while the density of states at the Fermi level remains finite.

1. Introduction

Experimental studies concerning the metal–insulator transition have been conducted in the past on heavily doped crystalline semiconductors [1, 2], amorphous semiconductors doped with transition metal elements [3–12], and granular metals consisting of small metallic particles embedded in an insulating matrix [13, 14]. In the first two groups, doped atoms are assumed to be randomly and homogeneously distributed either in a crystalline or in an amorphous matrix. On the other hand, metallic atoms in the granular metals are embedded as a cluster, of diameter of about 30 Å, in a semiconducting matrix. Hence, their distribution is heterogeneous. The metal–insulator transition has been discussed on more or less the same footing regardless of whether the distribution of doped atoms is homogeneous or heterogeneous [15]: the variable-range hopping mechanism on the insulating side, and weak-localization effects on the metallic side.

Amorphous M_xSi_{100-x} or M_xGe_{100-x} alloys can be relatively easily formed, either by vapour deposition or by the sputtering technique, when M is chosen from the transition

0953-8984/97/255333+21$19.50

metal elements, e.g. Au–Ge [3], Au–Si [4], Nb–Si [5], Cr–Si [6], Cr–Ge [7], Ni–Si [8, 9], Pd–Si [10], Ta–Si [11], and V–Si [12]. Amorphous Si or Ge alloys have been claimed to be advantageous over heavily doped crystalline semiconductors, since an amorphous single phase can be formed over a wide composition range across a critical composition associated with the metal–insulator transition. Experimental studies so far reported have largely concentrated on a change in the electron transport properties occurring upon the transition from metallic to activated hopping conduction. A change in the scattering mechanism has been generally discussed, without much attention being called to the distribution of metal atoms in an amorphous matrix.

Recently, however, Regan *et al* [16] pointed out the existence of the phase-separated region in amorphous Mo–Ge and Fe–Si alloys through the observation of small-angle x-ray scattering spectra. They showed that the size of the metallic clusters extends to the order of 10 Å in the growth plane, and 15–20 Å in the growth direction of the sputtered film samples. Hence, the system may be similar to that of the granular metals. They suggested that such nano-scale segregation of metallic clusters would explain the finite electronic specific heat coefficient observed in the insulating regime ($x < 10$) of the amorphous Mo_xGe_{100-x} alloys [17]. Thus, one cannot draw a conclusion as to whether the observed finite density of states at the Fermi level simply reflects the metallic character of a cluster or the localized state inherent to a 'homogeneous' amorphous structure. Therefore, the detailed structural characterization of amorphous alloys employed for studies of the metal–insulator transition must be important.

Only limited work has been so far reported concerning the composition dependence of the atomic structure [9] and electronic structure [10] across the metal–insulator transition. Unfortunately, however, no comparison has been made with the electron transport properties. We consider it to be crucially important to study the atomic structures, electronic structures, and electron transport properties together, by using the same samples or samples prepared under the same preparation conditions.

In the present studies, we employed a series of amorphous V_xSi_{100-x} thick films ($7 \leqslant x \leqslant 74$) prepared by DC sputtering, and studied the interrelation of the atomic structures, electronic structures, electron transport, and magnetic properties to gain a comprehensive understanding of the metal–insulator transition. The local atomic structure was investigated by means of a combination of the neutron and x-ray diffraction techniques, and the electronic structure by means of x-ray photoemission spectroscopy (XPS) and soft-x-ray emission spectroscopy (SXS). Quantitative information about the density of states at the Fermi level was derived from the electronic specific heat measurements. As regards the electron transport properties, the temperature dependence of the electrical resistivity was measured in the range 2–300 K.

2. Experimental procedure

An alloy ingot was prepared in button form, 30 mm in diameter and 7 mm in thickness, by arc melting appropriate amounts of pure Si shot (99.9999%) and pure V flakes (99.95%). The button-shaped ingot was directly used as a target for the triode DC sputtering. The chamber was baked at 120 °C for about 20 h in vacuum, and then the background pressure was reduced to 6×10^{-8} Torr before the introduction of pure Ar gas was carried out. A Cu plate was used as a substrate. During deposition, the Ar gas pressure was maintained at 8×10^{-3} Torr. The distance between the target and substrate was adjusted to 2.5 cm. The sputtering rate was about 700 Å min^{-1}. The deposition was continued for about 72 h until the film thickness reached about 300 μm. A thick film was mechanically removed from the

substrate without difficulty.

The x-ray diffraction spectra were taken with Cu Kα radiation. The formation of an amorphous single phase was confirmed by examining the appearance of just the halo pattern, without any Bragg peaks. The composition of the amorphous samples was checked by means of an energy-dispersive x-ray analyser (Seiko Instruments, SII). The deviation from the nominal composition was found to be within $\pm 1\%$. In addition, no measurable difference in composition was observed between the top and bottom surfaces of the sample. We could confirm that an amorphous single phase was obtained in this experiment from $x = 7$ up to $x = 74$ in the V_xSi_{100-x} systems. The formation of an amorphous phase was also checked by using a differential scanning calorimeter (RIGAKU-8131BH). Each sample, weighing approximately 10–20 mg, was sealed in a Ag pan and heated in an Ar gas flowing atmosphere with a heating speed of 15 K min^{-1} in the temperature range up to 800 °C. The mass density was measured using toluene as the working fluid in the Archimedes method.

The structure factor and the radial distribution functions (RDF) were determined by using a combination of x-ray and neutron diffraction techniques. Mo Kα radiation (50 kV and 30 mA) was employed in the step-scanning mode in the x-ray diffraction experiment. On the other hand, the neutron diffraction spectra were taken, using the High Intensity Total (HIT-II) scattering spectrometer, at the National Laboratory for High Energy Physics, Tsukuba, Japan. The sample was crushed into small pieces, and packed into a cylindrical container made of vanadium, 40 mm in height, 8 mm in inner diameter, and 25 μm in wall thickness. The data were accumulated for up to about 15–20 h for the sample plus its container, and the contribution of the container was subsequently subtracted.

The XPS valence band spectra were taken using an Al Kα monochromated x-ray beam (Surface Science Instrument, X-probe). The Fermi level was calibrated using a pure Au film as a reference. The Si Kβ and V Lα SXS spectra correspond to the radiation emitted upon the transition from the Si 3p band to its 1s level and from the V 3d band to its 2p level, and provide information about Si 3p and V 3d valence band structure, respectively (Shimazu, EPMA 8705). The Fermi level in the Si Kβ SXS spectra was determined by measuring both the XPS Si 2p level and Si Kα radiation corresponding to the transition from Si 2p to 1s states. Similarly, the Fermi level in the V Lα spectra can be determined by measuring the XPS V 2p level.

Table 1. Electronic properties of amorphous V_xSi_{100-x} alloys. γ: the electronic specific heat coefficient; Θ_D: the Debye temperature; δ: the magnetic specific heat coefficient in equation (11); $\rho_{300\,K}$: the resistivity at 300 K; and d: the mass density.

x	γ (mJ mol^{-1} K^{-2})	Θ_D (K)	δ (mJ K mol^{-1})	$\rho_{300\,K}$ ($\mu\Omega$ cm)	d (g cm^{-3})
7	0.28	332	2.3	2.1×10^6	2.243
12	0.37	406	1.5	1.8×10^5	2.603
14	0.57	393	—	7.2×10^4	2.694
17				2.0×10^4	2.807
21	0.98	432	—	5.3×10^3	2.991
29	1.42	506	—	1.9×10^3	3.338
37	1.87	467	—	830	3.873
43	2.14	506	—	440	
53	3.22	417	—	332	
74	3.61	427	—	223	

The low-temperature specific heat was measured in the temperature range 1.6–5.5 K, using a DC adiabatic method. A finely crushed sample, about 0.02–0.04 mol in weight, was compacted into a Au-plated Cu container. The specific heat of the sample was deduced by subtracting the contribution of the container. The electrical resistivity was measured in the DC four-terminal method in the temperature range 2–300 K. However, the measurement was limited to down to about 50 K for the $x = 7$ sample, because of an increase in resistivity beyond several Ω cm with decreasing temperature. The sample for the resistivity measurement was prepared using the same method as described above, but a quartz substrate was used in place of the Cu plate. The film thickness was limited to about 2–4 μm, since further deposition led to crystallization, because of the poor thermal conductivity of the quartz substrate. To allow a precise determination of the sample geometry to be made, we used a mask having a rectangular deposition area, 4 mm in width and 6 mm in length, between two voltage terminals. A Talysurf stylus was used to measure the film thickness with the accuracy of $\pm 5\%$ (Dektak IIA, Sloan Incorporated). The low-temperature specific heat coefficients, the resistivity at 300 K, and the mass density are listed in table 1.

Table 2. Magnetic data for the amorphous V_xSi_{100-x} alloys. C: the Curie constant per mole; Θ: the characteristic temperature; C_V: the Curie constant per mole of vanadium; and p: the effective Bohr magneton per V atom.

x	C (emu mol^{-1})	Θ (K)	C_V (emu/(mol V))	p
7	3.2×10^{-4}	4.7	4.57×10^{-3}	0.18
12	2.9×10^{-4}	−1.7	2.42×10^{-3}	0.14

The magnetic susceptibility was measured in the temperature range 2–250 K for representative samples, using a SQUID magnetometer (QUANTUM DESIGN MPMS-7) under a magnetic field of 2000 Oe. The data, after subtracting a temperature-independent term, were fitted to the Curie–Weiss law. The relevant numerical values are listed in table 2.

3. Results and discussion

3.1. Electron transport properties

Figure 1 shows the temperature dependence of the conductivity on a logarithmic scale for representative amorphous V_xSi_{100-x} alloys. The change in the conductivity with decreasing temperature is extremely large for samples with $x < 20$. The data may be analysed in the framework of the variable-range hopping model, and are fitted to the following equation:

$$\sigma(T) = \sigma_0 \exp[-(T_0/T)^n] \tag{1}$$

where σ_0, T_0, and n are fitting parameters. A value of $n = 1/4$ would be expected for a constant density of states near the Fermi level [18], while a value of $n = 1/2$ is predicted in the Coulomb gap model for a three-dimensional system [19]. Experimentally, the $n = 1/2$ fitting was apparently successful for the amorphous Cr–Si [6], Cr–Ge [7], and Ni–Si alloys [8], while the $n = 1/4$ fitting was employed for the amorphous V–Si alloys [12].

Equation (1) can be rewritten in the form

$$\mathrm{d}\ln\sigma(T)/\mathrm{d}\ln T = -n\,[\ln\sigma(T) - \ln\sigma_0]\,. \tag{2}$$

To test the validity of equation (1), we plotted the data from figure 1 for the $x = 7$ and $x = 14$ samples in the form of $\mathrm{d}\ln\sigma(T)/\mathrm{d}\ln T$ versus $\ln\sigma(T)$ in figure 2(a). The data

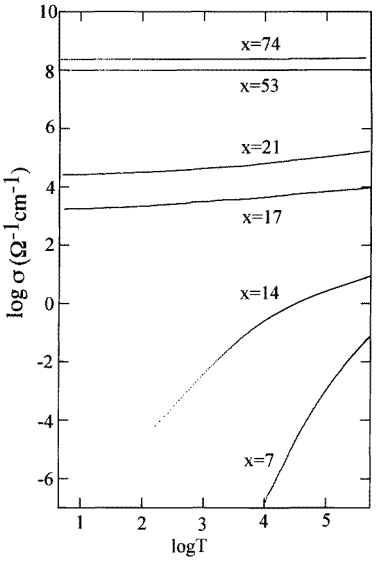

Figure 1. The temperature dependence of the conductivity on a log–log scale for a series of amorphous V_xSi_{100-x} alloys.

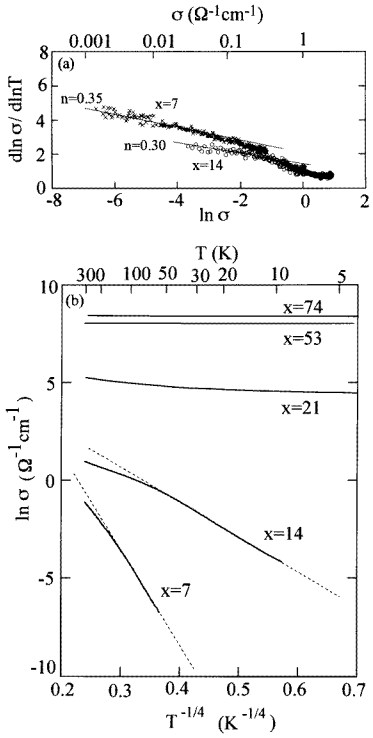

Figure 2. (a) $\mathrm{d}\ln\sigma/\mathrm{d}\ln T$ against $\ln\sigma$ for the $x = 7$ and $x = 14$ samples in the insulating regime. The data in the low-temperature range are fitted to straight lines with slopes of $n = 0.35$ and $n = 0.30$ for the $x = 7$ and $x = 14$ samples, respectively. (b) The $T^{-1/4}$-dependence of $\ln\sigma$ for a series of amorphous V_xSi_{100-x} alloys.

for low temperatures can be fitted to a straight line with slopes of 0.3–0.35 for the present samples. Although the experimentally derived exponent n deviates slightly from 1/4, we plotted the data against $T^{-1/4}$ in figure 2(b). Indeed, no significant difference is found according to whether the data are plotted against $T^{-1/4}$ or $T^{-0.33}$. It can be seen that the data apparently fall on a straight line below about 50 and 120 K for the $x = 14$ and $x = 7$ samples, respectively. We therefore conclude that the amorphous V_xSi_{100-x} alloys with $x \leqslant 14$ are in the insulating regime, and that their electron transport can be described by an activated hopping mechanism.

The temperature dependence of the conductivity in the metallic regime has been analysed in terms of weak-localization effects coupled with an enhanced electron–electron interaction, and is often expressed as

$$\sigma(T) = \sigma_0 + \alpha T \qquad (T > 30\ \mathrm{K}) \tag{3a}$$

and

$$\sigma(T) = \sigma_0 + \beta\sqrt{T} \qquad (T < 20\ \mathrm{K}). \tag{3b}$$

As shown in figure 3, the square-root temperature dependence is indeed observed below about 25 K for the amorphous V_xSi_{100-x} alloys with $x \geqslant 21$. We conclude from figures

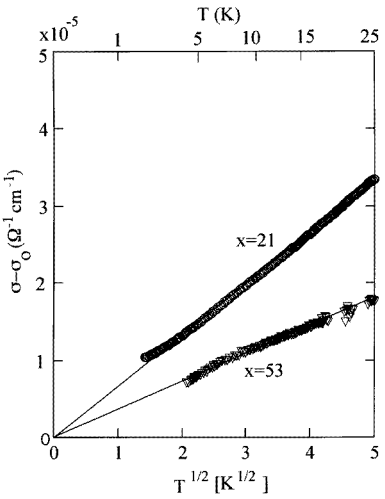

Figure 3. The $T^{1/2}$-dependence of the conductivity relative to that extrapolated to absolute zero for the samples with $x = 21$ and $x = 53$ in the metallic regime.

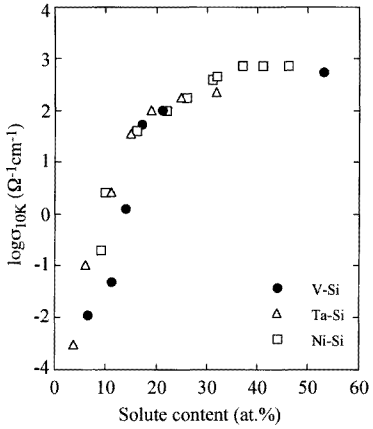

Figure 4. The conductivity at 10 K as a function of solute concentration for the Si-based amorphous alloys. The symbols show the results for the (●) V–Si, (△) Ta–Si [11], and (□) Ni–Si [8] alloys. The conductivity is shown on a logarithmic scale.

1–3 that the samples with $x \geqslant 21$ are in the metallic regime, whereas those with $x \leqslant 14$ are in the insulating regime. This is consistent with the data for amorphous V_xSi_{100-x} ($10 \leqslant x \leqslant 50$) alloys reported by Boghosian and Howson [12].

The value of the conductivity at 10 K can be read off from the data shown in figure 1, and is plotted as a function of the V concentration in figure 4. The value for the $x = 7$ sample was obtained by extrapolating the $T^{-1/4}$-behaviour down to 10 K. Also included are the literature data for the amorphous Ni–Si [8] and Ta–Si [11] alloys. It can be seen that the value of $\sigma_{10\,K}$ decreases with decreasing metal content along a universal curve, regardless of the atomic species of the transition metal involved. The metal–insulator transition has been suggested to occur when the conductivity crosses the value of 50 Ω^{-1} cm^{-1}. One can see from figure 4 that this corresponds to a transition metal concentration of 15–20 at.%. Therefore, both the temperature dependence of the conductivity and the composition dependence of $\sigma_{10\,K}$ are consistent with the conclusion that the critical concentration, across which the metal–insulator takes place in the amorphous V_xSi_{100-x} alloys, lies in the range $x = 15$–20.

3.2. Thermal properties

Figure 5(a) shows the DSC thermograms for a series of the amorphous V_xSi_{100-x} alloys. It is seen that a single exothermic peak was observed for samples with $x \leqslant 15$, while two successive peaks were observed for those with $x \geqslant 19$. The x-ray diffraction spectra for samples heated up above the exothermic peaks allowed us to identify the lower exothermic peak as indicating the crystallization into the VSi_2 compound, and the higher one as indicating that into Si. The crystallization temperature, which is marked by arrows in figure 5(a), is plotted in figure 5(b) as a function of V concentration. Data for amorphous Si prepared by the glow-discharge technique are available from the literature [20], and are included in figure 5(b) for comparison. It is clear that the VSi_2 compound precipitates for

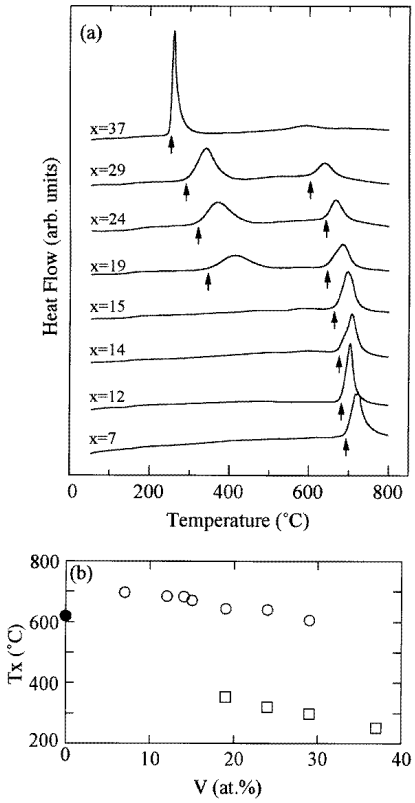

Figure 5. (a) DSC spectra for a series of the amorphous V_xSi_{100-x} alloys. The crystallization temperatures are determined from the arrows indicated. The amorphous alloys with $19 \leqslant x \leqslant 29$ exhibit two exothermic peaks. The x-ray diffraction studies of the region after the first peak revealed the growth of a VSi_2 compound. The structure after the second peak was clearly identified as a mixture of Si and VSi_2. (b) The crystallization temperature as a function of the V concentration in the present samples.

samples with $x \geqslant 19$, while the crystallization into Si occurs at a higher temperature and persists up to $x = 29$.

3.3. Atomic structures

Figures 6 and 7 show the structure factors derived from neutron and x-ray diffraction experiments for a series of amorphous V_xSi_{100-x} alloys, respectively. It is clear that no Bragg peaks exist in either set of data, indicating the lack of long-range order characteristic of an amorphous phase. One can further see in the neutron diffraction spectra that a small oscillation remains visible to high scattering wavenumbers, suggesting the existence of a local short-range order in the amorphous structure. Moreover, a substantial difference is seen between the neutron and x-ray structure factors. This is certainly due to the difference in the scattering amplitude or scattering factor of the constituent atoms V and Si for neutron and x-ray radiation.

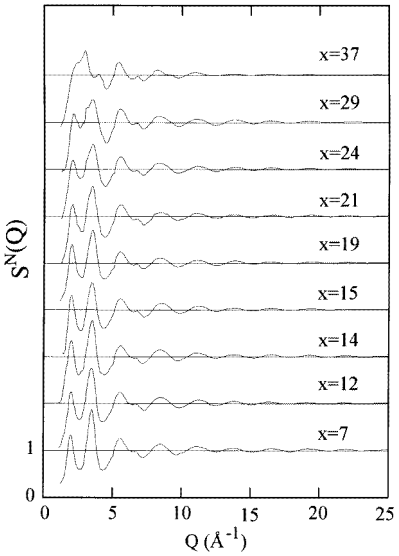

Figure 6. The structure factors $S^N(Q)$ derived from neutron diffraction studies for a series of amorphous V_xSi_{100-x} alloys.

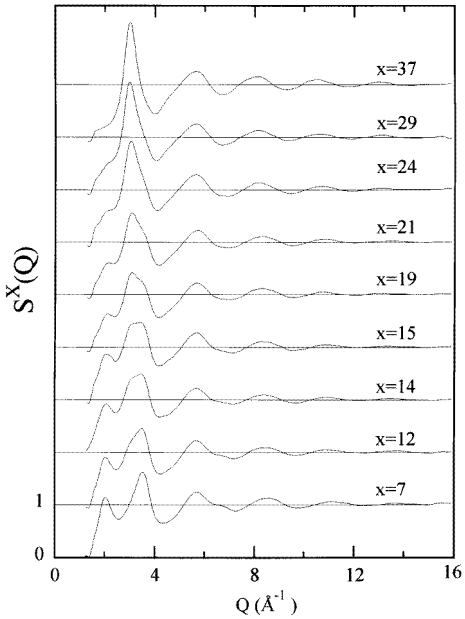

Figure 7. The structure factors $S^X(Q)$ derived from x-ray diffraction studies with Mo Kα radiation for a series of amorphous V_xSi_{100-x} alloys.

The total structure factor for the binary V–Si alloy is expressed as

$$S(Q) = \frac{1}{\langle b\rangle^2}\left\{c_{\mathrm{Si}}^2 b_{\mathrm{Si}}^2 S_{\mathrm{SiSi}}(Q) + 2c_{\mathrm{Si}}c_{\mathrm{V}}b_{\mathrm{Si}}b_{\mathrm{V}}S_{\mathrm{SiV}}(Q) + c_{\mathrm{V}}^2 b_{\mathrm{V}}^2 S_{\mathrm{VV}}(Q)\right\} \tag{4}$$

in the Faber–Ziman expression, and $\langle b\rangle$ is given by

$$\langle b\rangle = c_{\mathrm{Si}}b_{\mathrm{Si}} + c_{\mathrm{V}}b_{\mathrm{V}} \tag{5}$$

where c_i and b_i are concentration and scattering amplitude associated with i = Si atom or V atom, respectively. $S_{ij}(Q)$ represents the partial structure factor for the i–j atomic pair. The scattering amplitudes of V and Si atoms for a neutron beam are known to be -0.0382×10^{-12} cm and 0.4149×10^{-12} cm, respectively. On the other hand, the scattering factors of V and Si atoms for an x-ray photon beam are proportional to their atomic numbers, 23 and 14. For example, the neutron and x-ray total structure factors for the amorphous $V_{12}Si_{88}$ alloy can be expressed as

$$S^N(Q) = 1.025\,62\,S_{\mathrm{SiSi}}(Q) - 0.025\,78\,S_{\mathrm{SiV}}(Q) + 0.000\,16\,S_{\mathrm{VV}}(Q) \tag{6}$$

$$S^X(Q) = 0.521\,04\,S_{\mathrm{SiSi}}(Q) + 0.348\,41\,S_{\mathrm{SiV}}(Q) + 0.050\,51\,S_{\mathrm{VV}}(Q). \tag{7}$$

By eliminating $S_{\mathrm{SiV}}(Q)$ from equations (6) and (7), we obtain

$$S_1(Q) \equiv 0.9362\,S^N(Q) + 0.069\,27\,S^X(Q) = 0.9963\,S_{\mathrm{SiSi}}(Q) + 0.0036\,S_{\mathrm{VV}}(Q). \tag{8}$$

Equation (8) indicates that the contribution from the V–V atomic pair amounts to only 0.3% in $S_1(Q)$. This contribution certainly increases with increasing V concentration, but reaches only 5% even for the $x = 37$ sample. Thus, we say that $S_1(Q)$ represents well the Si–Si correlation. Likewise, we obtain

$$S_2(Q) = 0.904\,38\,S_{\mathrm{SiV}}(Q) + 0.095\,62\,S_{\mathrm{VV}}(Q) \tag{9}$$

if $S_{SiSi}(Q)$ is eliminated from equations (6) and (7). The contribution of $S_{VV}(Q)$ in equation (9) is about 10% of the total $S_2(Q)$, but reaches 31% for the V-richest sample, with $x = 37$.

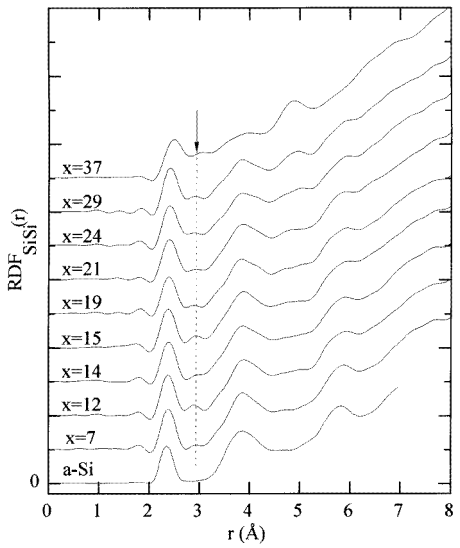

Figure 8. The radial distribution function (RDF) obtained by the Fourier transformation of equation (8) for a series of amorphous V_xSi_{100-x} alloys. The dashed line with an arrow indicates the peak at 2.9 Å.

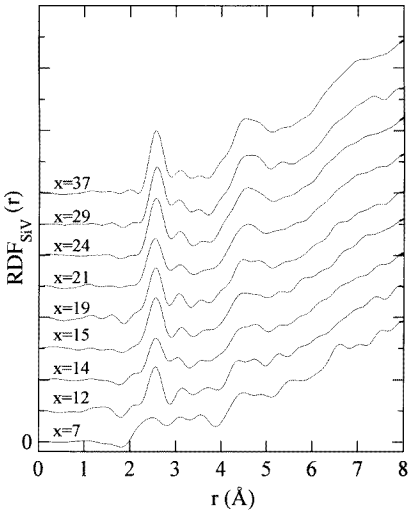

Figure 9. The radial distribution function (RDF) obtained by the Fourier transformation of equation (9) for a series of amorphous V_xSi_{100-x} alloys.

The radial distribution function (RDF) spectra can be calculated by Fourier transforming $S_1(Q)$ and $S_2(Q)$, both of which were truncated at the wavenumber $Q_{max} = 15.5$ Å^{-1}. Note that here both $S_1(Q)$ and $S_2(Q)$ are derived as linear combinations of the x-ray and neutron total structure factors, and, hence, the Q_{max}-value is limited by a smaller one; Q_{max} turned out to be about 15.5 and 23 Å^{-1} for the present x-ray and neutron diffraction measurements, respectively. Since $S_1(Q)$ and $S_2(Q)$ mainly represent the Si–Si and Si–V correlations, the RDF spectra shown in figures 8 and 9 are denoted as $RDF_{SiSi}(r)$ and $RDF_{SiV}(r)$, respectively, in the following discussion.

First, we discuss the $RDF_{SiSi}(r)$ spectra shown in figure 8, into which the data for amorphous Si reported by Fortner and Lannin [21] are incorporated. It can be seen that the first peak at about 2.4 Å remains almost unchanged with increasing V concentration. But a small peak at about 2.9 Å, marked by a dashed line with an arrow, is found to grow when V atoms are introduced. Its position agrees with the Si–Si distance in the hexagonal VSi_2 compound [22]. This should reflect the distortion of the Si network upon introduction of V atoms.

The $RDF_{SiV}(r)$ spectra show a unique V concentration dependence, as can be seen from figure 9. In particular, the spectrum for the $x = 7$ sample is substantially different from the remaining ones. But a new local atomic structure is gradually built up, as x exceeds about 10, and is apparently stabilized above $x = 20$. We have already pointed out that the VSi_2 compound precipitates for the $x > 20$ samples, when heated above the crystallization temperature. This suggests that the local atomic structure for the amorphous alloys with $x > 20$ would be similar to that of the hexagonal VSi_2 compound.

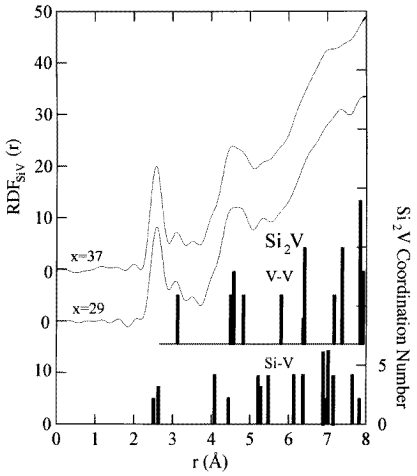

Figure 10. A comparison of $RDF_{SiV}(r)$ for the $x = 29$ and $x = 37$ samples with the local atomic structure of the VSi_2 intermetallic compound.

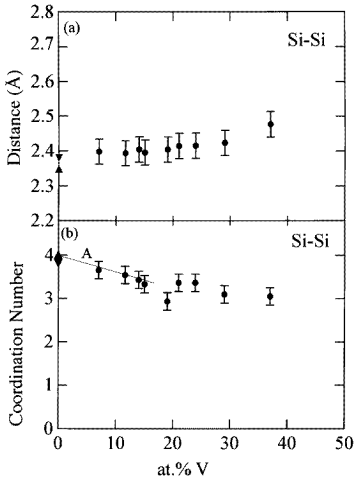

Figure 11. (a) The Si–Si nearest-neighbour atomic distance and (b) the corresponding coordination number as functions of the V concentration for the amorphous V_xSi_{100-x} alloys. The line A is drawn for the tetrahedrally bonded Si network model by connecting the coordination numbers 4 and 3 at 0 and 25 at.% V, respectively.

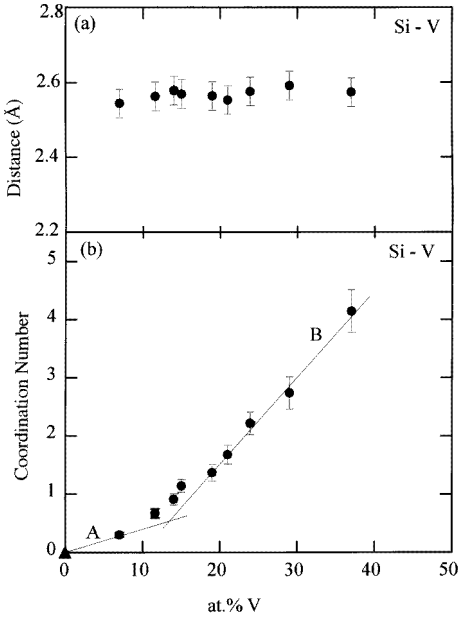

Figure 12. (a) The Si–V nearest-neighbour atomic distance and (b) the corresponding coordination number as functions of the V concentration for the amorphous V_xSi_{100-x} alloys. The line A corresponds to the line A in figure 11. The line B is drawn through the data points in the range $19 \leqslant x \leqslant 37$.

The VSi_2 compound has a layered structure possessing both Si–Si and Si–V pairs at 2.50 and 2.63 Å, and V–V pairs at 3.12 Å [22]. The RDF spectra for the samples with $x = 29$ and $x = 37$ are compared with the atomic position and coordination number associated with Si–V and V–V pairs in the VSi_2 compound. Remember here that the V–V correlation for the samples with $x = 29$ and $x = 37$ is no longer negligible, but amounts to about 30% in

$S_2(Q)$. Indeed, as shown in figure 10, the major peaks observed in the RDF spectra are quite consistent with the local atomic structure of the VSi_2 compound, and the peaks associated with Si–V and V–V pairs are fortunately well separated. In the VSi_2 compound, Si atoms are always surrounded by five Si atoms and five V atoms, and V atoms are surrounded by ten Si atoms. Hence, the coordination number around Si and V atoms is always ten, in sharp contrast to the value of four for amorphous Si. This means that an amorphous alloy possessing the VSi_2-like local atomic structure is typical of a metallic glass, and can be differentiated from the amorphous Si-like structure.

The first peak in the $RDF_{SiSi}(r)$ and $RDF_{SiV}(r)$ spectra shown in figures 8 and 9 is fitted to the Gaussian function to deduce quantitatively the nearest-neighbour distance and its coordination number. The results for Si–Si and Si–V correlations are plotted as functions of V concentration in figures 11 and 12. Let us first discuss the data for the Si–Si correlation. Included also are the data for crystalline and amorphous Si from the literature [21]. The Si–Si atomic distance remains unchanged within the accuracy of the measurement up to about $x = 30$, whereas the coordination number decreases more or less linearly up to $x = 15$. A line labelled A is drawn through the data points in this composition range. This line intercepts the coordination number 4 at $x = 0$, and passes the coordination number 3 at $x = 25$. This means that a quarter of the Si atoms in the tetrahedrally bonded network are substituted for with V atoms at $x = 25$. Indeed, the data at least up to $x = 15$ fall on this line, suggesting that the semiconducting Si network, over which V atoms are randomly distributed, is a characteristic structural feature in the V-poor amorphous alloys. Here it must be noted that the Si–Si bonding in the tetrahedral network is certainly disrupted, and is distorted by the introduction of the V atoms, resulting in the formation of the new Si–Si correlation at 2.9 Å as is evident from the $RDF_{SiSi}(r)$ spectra shown in figure 8.

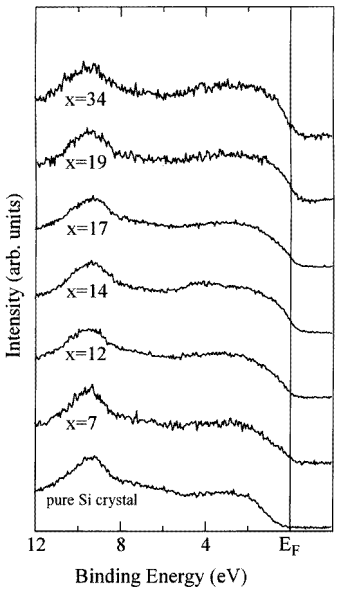

Figure 13. XPS valence band spectra for a series of amorphous V_xSi_{100-x} alloys.

The Si–V atomic distance shown in figure 12 is found to be about 2.56 Å, and to be almost independent of the V concentration. However, the coordination number shows a unique behaviour. The VSi_2 compound possesses two different Si–V atomic pairs at 2.50 and 2.63 Å, and their coordination numbers are 2 and 3, respectively. The observed Si–V

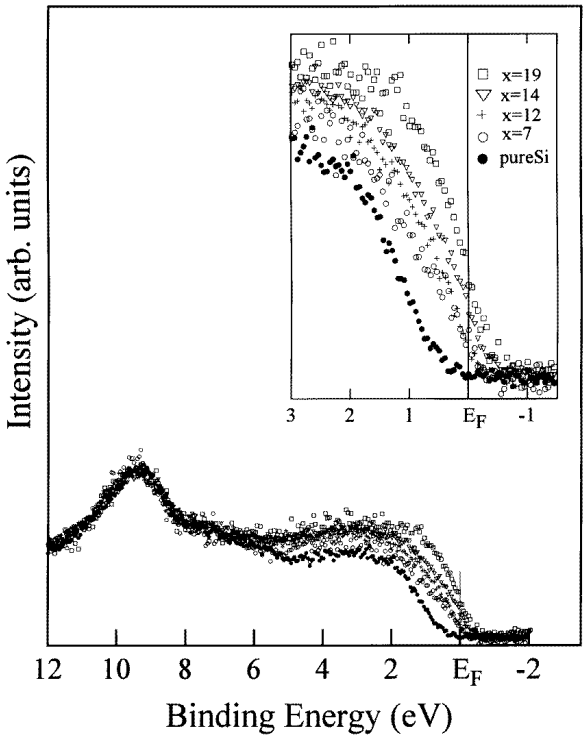

Figure 14. XPS valence band spectra on an expanded scale for a series of amorphous V_xSi_{100-x} alloys. The inset shows a further expansion near the Fermi level.

atomic distance of 2.56 Å, for the $x = 37$ sample, whose V concentration is near that of the VSi_2 compound, is close to the average for these two sites in the compound. The coordination number for the $x = 37$ sample is 4.2, which is close to 5 in the compound. The line B can be drawn through the data points for samples with $x > 20$. This line represents a change in the coordination number of amorphous V_xSi_{100-x} alloys with $x > 20$, the local structure of which is characterized by the VSi_2 compound.

As discussed above, the Si network model was applied to the V-poor amorphous alloys. The line corresponding to A in figure 11 should pass through the origin and 1 at $x = 25$ in the Si–V correlation shown in figure 12. This is again denoted as A, and is drawn in figure 12. It is seen that only the data points for the $x = 7$ sample happen to fall on this line, but those for $x = 12$, 14, and 15 deviate upwards from this line. The latter deviate not only from the line A but also from the line B. We believe, therefore, that this is the region where the Si network and VSi_2 metallic glass-like structures are competing with each other, and where the structural frustration occurs. It is in this transition region that the metal–insulator transition occurs. Asal *et al* [9] studied the local atomic structure in amorphous Ni–Si alloys by the EXAFS technique, and pointed out that the tetrahedral network structure changes to a higher-coordination metallic structure when the Ni content exceeds 20 at.%.

In summary, the present structural analysis for the amorphous V_xSi_{100-x} alloys demonstrated that the tetrahedrally bonded Si network structure, into which V atoms are randomly substituted, persists up to about 10 at.% V, and that it changes to a metallic glass structure, which locally resembles that of the VSi_2 intermetallic compound, when x exceeds

about 20 at.%. The composition range $10 < x < 20$ corresponds to a region where these two local atomic structures are apparently competing with each other, and the metal–insulator transition takes place.

3.4. Electronic structures

We have studied in the preceding section how the atomic structure changes across the metal–insulator transition region. A main objective in this section is to examine how the electronic structure near the Fermi level changes across this critical composition range. For this particular purpose, we employed a combination of the XPS and SXS techniques, and also electronic specific heat measurements. Figure 13 shows the XPS valence band spectra for a series of amorphous V_xSi_{100-x} alloys. The Si spectrum was taken by using pure Si crystal. One can clearly see the existence of the energy gap in pure Si. A peak at about 10 eV can be attributed to Si 3s states. Tanaka *et al* [10] also interpreted the peak at 9.2 eV observed in their UPS spectra for the amorphous Pd–Si alloys as arising from the Si 3s state. As can be seen from figure 13, the density of states immediately below the Fermi level gradually increases with increasing V concentration, indicating a gradual transition to a metallic substance. To extract more detailed information near the Fermi level, we show the XPS spectra just in the energy range from the Fermi level down to 3 eV in figure 14. The density of states at the Fermi level apparently becomes finite even for the sample with $x = 7$, and increases with increasing V concentration. In the case of the amorphous Pd–Si alloys, the density of states at the Fermi level becomes finite at 13 at.% Pd [10].

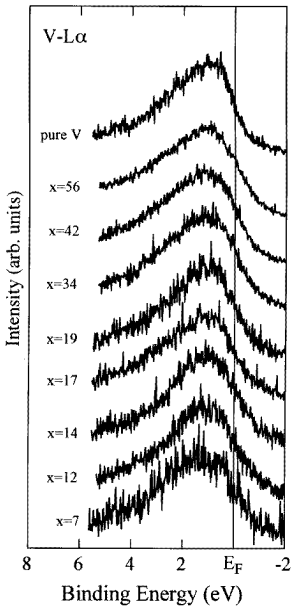

Figure 15. V Lα SXS spectra for a series of amorphous V_xSi_{100-x} alloys.

It is of great interest to study which electronic states are responsible for filling the gap at the Fermi level. Figure 15 shows the V Lα SXS spectra for a series of the amorphous V_xSi_{100-x} alloys. As mentioned in section 2, the V Lα spectra reflect mainly the V 3d states. It is clear from figure 15 that the V 3d states appear immediately below the Fermi level even for the $x = 7$ sample, and its position remains almost unchanged with increasing

V concentration. We conclude from this that the V 3d states fill the energy gap at the Fermi level. It must be emphasized that a finite density of states is apparently formed even at $x = 7$, where the electron transport properties definitely prove this sample to be in the insulating regime.

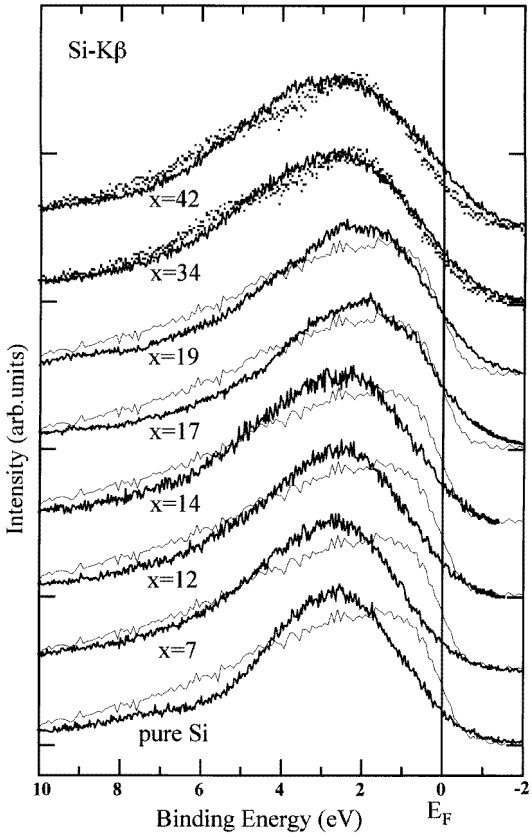

Figure 16. Si Kβ SXS spectra (thick lines) for a series of amorphous V_xSi_{100-x} alloys. Superimposed are the data for pure Al (thin lines) and the VSi_2 intermetallic compound (dots). The $x = 34$ spectrum resembles well that of the VSi_2 compound.

The Si Kβ spectra are shown in figure 16 for a series of the amorphous V_xSi_{100-x} alloys. As mentioned in section 2, the Si Kβ spectra represent the Si 3p electron distribution. First of all, it can be seen that the width of the Si Kβ spectrum for pure Si is much narrower than that of the free-electron-like Al Kβ spectrum, which is shown as a thinner curve after adjusting the Fermi level. This is a clear indication that the pure Si 3p band forms a narrow band, characteristic of the covalent bonding. As is clear from figure 16, the Si 3p band is gradually widened with increasing V concentration as a result of the hybridization between V 3d and Si 3p states. It is also interesting to note that the spectrum for the $x = 34$ sample resembles well that of the VSi_2 compound.

More quantitative information regarding the density of states at the Fermi level can be drawn from the measurements of the electronic specific heat coefficient. The low-temperature specific heat data are shown in figure 17 in the form of C/T versus T^2 for the present samples. The scatter of the data points is rather large because of the limited number

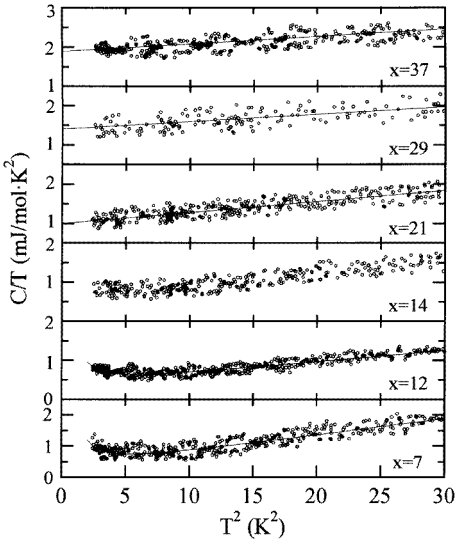

Figure 17. Low-temperature specific heat data in the form of C/T versus T^2 for a series of amorphous V_xSi_{100-x} alloys. A clear upturn is visible for the $x = 7$, 12, and 14 samples.

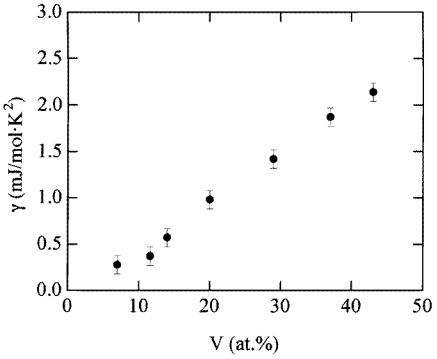

Figure 18. The electronic specific heat coefficient γ as a function of the V concentration for a series of amorphous V_xSi_{100-x} alloys.

of samples. Except for the samples with $x \leqslant 14$, the data fall on a straight line, and can be fitted to the equation

$$C = \gamma T + \alpha T^3 \tag{10}$$

where γ and α represent the linearly temperature-dependent specific heat coefficient and lattice specific heat coefficient, respectively. The numerical data are listed in table 1.

It may be recalled that the linearly temperature-dependent specific heat appears even in an amorphous insulator, because of the two-level configurational effect inherent to a disordered lattice [23]. But its magnitude is known to be of the order of 10^{-3} mJ g^{-1} K^{-2}, and may well be neglected in the present argument. Hereafter we assume the measured value of γ to represent the electronic specific heat coefficient. The electronic specific heat coefficient γ is plotted in figure 18 as a function of V concentration. First of all, it is important to compare the present results with the data for the VSi_2 compound reported by Lasjaunias *et al* [24]. A high value of $\gamma = 2.02$ mJ mol^{-1} K^{-2} for the VSi_2 compound indicates that this compound is indeed a metal. A reasonable agreement with the value for the $x = 29$ sample, and its subsequent linear decrease with decreasing V concentration down to $x = 20$, are consistent with our conclusion that the samples with $x > 20$ have a VSi_2-like local atomic structure. A linearly temperature-dependent specific heat coefficient was not detected for amorphous Si [25]. This indicates the absence of the electronic specific heat coefficient for amorphous Si. In contrast, the value of γ is definitely finite for the $x = 7$ sample, despite the fact that this sample is in the insulating regime.

A finite value of γ has been reported in the composition range $x < 10$ for the amorphous Mo_xGe_{100-x} alloys [17]. However, Regan *et al* [16] showed evidence for the presence of Mo clusters in the amorphous Ge matrix through small-angle scattering experiments. They suggested that metallic clusters might be responsible for the observed finite value of γ for the insulating regime in this system. In contrast, the present atomic structure analysis for

samples with $x < 10$ demonstrated the validity of the Si network model with a random substitution of V atoms for Si atoms. It may also be worth mentioning that, as opposed to the case for the data reported for the amorphous Mo_xGe_{100-x} alloys, no measurable enhancement in the intensities has been observed down to Q-values of 0.5 $Å^{-1}$ in the present neutron diffraction structure factor. This means that the local atomic structures in the present amorphous V_xSi_{100-x} alloys with $x < 10$ are entirely different from those reported for the Mo–Ge and Fe–Si alloys. We conclude, therefore, that precipitation of V clusters is absent, and that V atoms are distributed randomly and homogeneously in the tetrahedrally bonded Si network, and also that the finite size of the density of states at the Fermi level in the insulating regime is caused by the V 3d states in the V atom hybridized with surrounding Si 3p states. It must also be emphasized that the states formed at the Fermi level are indeed localized, as is proved by the electron transport data shown in figures 1–3.

3.5. Magnetic properties

The low-temperature specific heat data shown in figure 17 show an upturn deviation from a straight line for samples with $x = 7$ and $x = 12$. The low-temperature specific heat data having such an upturn may be fitted to

$$C = \gamma T + \alpha T^3 + \delta T^{-2} \tag{11}$$

where δ is the magnetic specific heat coefficient. Though a very weak upturn is also visible for the $x = 14$ sample, the least-squares fitting for this sample was made using equation (10) because of a large scatter of the data points. The numerical data thus obtained are listed in table 1. This suggests that there is a magnetic contribution in the V-poor alloys in the insulating regime.

Figure 19 shows the temperature dependence of the magnetic susceptibility for several amorphous V_xSi_{100-x} alloys. The magnetic susceptibility for the VSi_2 intermetallic compound has been reported by Gottlieb *et al* [26]. They reported that it is essentially temperature independent over the range 4–300 K, and about 4.5 and 3.0 (in units of 10^{-5} emu mol^{-1}) for the directions of the magnetic field parallel and perpendicular to the c-axis of the hexagonal structure, respectively. The present result for the $x = 37$ sample is indeed consistent with the data for the VSi_2 compound. It is clear from figure 19 that the amorphous alloy with $x = 37$ is non-magnetic, since temperature dependence of the magnetic susceptibility is essentially absent. However, a strong temperature dependence appears at low temperatures, and the temperature-independent contribution decreases sharply with decreasing V concentration, particularly upon entering the insulating regime.

The magnetic susceptibility data are fitted to the equation

$$\chi = \chi_0 + \frac{C}{T - \Theta} \tag{12}$$

where C, Θ, and χ_0 are fitting parameters. The data are plotted in figure 20, in the form of $1/(\chi - \chi_0)$ against temperature, by using the value of χ_0 discussed below. It can be seen that the data—at least, for the $x = 7$ and $x = 12$ samples—obey the Curie–Weiss law. The effective Bohr magneton p can be calculated from the Curie constant C by assuming that each V atom carries a magnetic moment. As listed in table 2, the characteristic temperature Θ is very close to zero, but becomes definitely positive for $x = 7$. The effective Bohr magneton is found to be 0.18 per V atom, which is much smaller than the value of 3.85 for a V^{2+} ion carrying three 3d electrons. This suggests that the hybridization of V 3d states with Si 3p states is substantial.

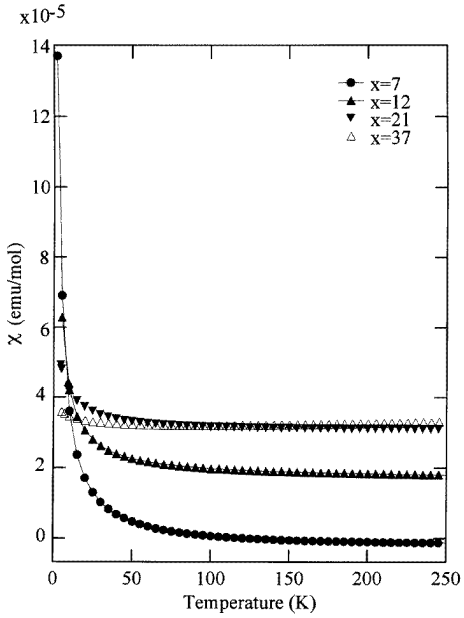

Figure 19. The magnetic susceptibility χ as a function of the temperature for the amorphous V_xSi_{100-x} alloys.

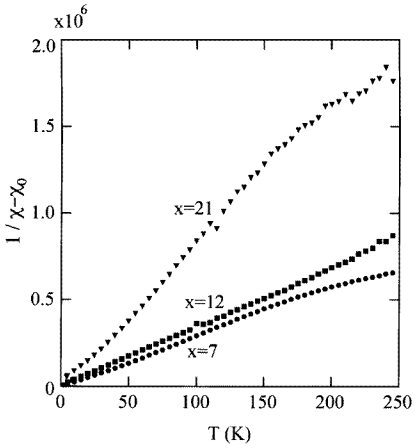

Figure 20. $1/(\chi - \chi_0)$ against the temperature for the amorphous V_xSi_{100-x} alloys. χ_0 represents a temperature-independent term.

The temperature-independent term χ_0 is expressed in the form

$$\chi_0 = \chi_{\text{core}} + \chi_{\text{el}} \tag{13}$$

where χ_{core} is the diamagnetic susceptibility of the core electrons, and χ_{el} represents the electronic contribution arising from the Pauli paramagnetism, the Landau diamagnetism, and the electron–electron interaction. The core-electron contribution χ_{core} is calculated by taking a weighted mean of $\chi_{\text{Si}} = -14 \times 10^{-6}$ emu mol^{-1} and $\chi_{\text{V}} = -21 \times 10^{-6}$ emu mol^{-1} in the same manner as was employed by Gottlieb *et al* for the VSi_2 compound [26].

Table 3. The density of states at the Fermi level deduced from temperature-independent magnetic susceptibility and electronic specific heat coefficient for amorphous V_xSi_{100-x} alloys.

x	χ_0 (10^{-6} emu mol^{-1})	χ_{ion} (10^{-6} emu mol^{-1})	χ_{el} (10^{-6} emu mol^{-1})	$N(E_F)_\chi$ (states eV^{-1}/atom)	γ_{exp} (mJ mol^{-1} K^{-2})	$N(E_F)_\gamma$ (states eV^{-1}/atom)	$N(E_F)_\chi/N(E_F)_\gamma$
7	−1.5	−14.5	13.0	0.40	0.28	0.12	3.3
12	17.6	−14.8	32.4	1.00	0.37	0.16	6.2
21	30.8	−15.5	46.3	1.43	0.98	0.42	3.4
37	33.5	−16.6	50.1	1.55	1.87	0.79	2.0

As can be seen from figure 19, the temperature dependence of the magnetic susceptibility is negligibly small above about 200 K for all of the samples studied. Hence, we subtracted the core-electron contribution from the measured magnetic susceptibility at 250 K, and attributed the remainder to the electronic contribution χ_{el}. By assuming that the magnitude of the Landau diamagnetism is given by one third of the Pauli paramagnetism, we calculated

the density of states at the Fermi level through the equation

$$\chi_{\rm el} = \chi_0 - \chi_{\rm core} = \frac{2}{3}\mu_B^2 N(E_F) \tag{14}$$

where μ_B is the Bohr magneton. The $N(E_F)$ values thus derived are listed in table 3, along with the values derived from the measured electronic specific heat coefficient $\gamma_{\rm exp}$ through the equation

$$\gamma_{\rm exp} = \left(\frac{\pi^2 k_B^2}{3}\right) N(E_F).$$

The ratio of the $N(E_F)$ derived from the magnetic susceptibility to that derived from the electronic specific heat coefficient is known as the Wilson ratio. The electron–electron interaction leads to a Wilson ratio equal to two in the absence of Stoner enhancement [27]. It is seen from table 3 that the ratio is almost two for the $x = 37$ sample, indicating the absence of Stoner enhancement for this non-magnetic alloy. However, the ratio tends to increase with decreasing V concentration, and exceeds three in the insulating regime. This may be taken as another indication for an enhancement in the exchange coupling between the V atoms with decreasing V concentration.

4. The metal–insulator transition in the $\rho - \gamma$ plot

The electrical conductivity σ_0 at absolute zero and the residual resistivity ρ_0 in the metallic conduction regime can be written down using the Drude expression:

$$\sigma_0 = \rho_0^{-1} = \frac{e^2}{3}\Lambda_F v_F N(E_F) \tag{15}$$

where $N(E_F)$, Λ_F, and v_F are the density of states, the mean free path, and the group velocity of the electrons at the Fermi level E_F. Mizutani [28] plotted the residual resistivity ρ_0 against the electronic specific heat coefficient γ for the large number of amorphous alloys studied so far, and pointed out that a high-resistivity limiting curve, above which no metallic data appear, can be drawn on the ρ_0–γ diagram. Note here that the value of γ represents $N(E_F)$ in equation (15).

When the mean free path Λ_F becomes comparable to an average atomic distance a, the wave vector k is no longer a good quantum number. Then, the group velocity $v = \hbar^{-1}\,{\rm d}E/{\rm d}k$ at the Fermi level loses its clear meaning [29]. Electrons in such a high-resistivity regime may be more properly described in terms of diffusional motion, without relying on the concepts of the mean free path and the Fermi velocity. The diffusion coefficient D is defined as the product $D = \frac{1}{3}\Lambda_F v_F$ in equation (15). In other words, the decomposition into Λ_F and v_F becomes meaningless at $\Lambda_F \approx a$. It has been assumed that the experimentally drawn high-resistivity limiting curve reflects the existence of a minimum diffusion coefficient for the metallic conduction [28]. The diffusion coefficient D takes a value of about 0.25 cm^2 s^{-1} for its possible minimum metallic conduction. Indeed, almost all high-resistivity metallic glasses characterized by weak-localization effects fall immediately below a ρ_0 versus γ curve with a constant D-value of 0.25 cm^2 s^{-1} [28].

An insulating regime may be approached by two different routes: in the first case, $N(E_F)$ is reduced to zero and, in the second case, D is reduced to zero, while $N(E_F)$ remains finite. The former case can, for instance, be realized when a band having holes in the Brillouin zone is filled with electrons. There exist systems like amorphous Ag–Cu–Ge alloys, in which $N(E_F)$ or the g-factor decreases with increasing Ge concentration, and the conductivity is well described by a scaling with the square of the g-factor [28]. This means

that not only $N(E_F)$ but also D is scaled in terms of the g-factor. Therefore, we say that amorphous alloy systems which obey the g^2-scaling in the approach to an insulating regime fall into the first-case group. In the second case, the value of σ_0 diminishes while $N(E_F)$ is kept finite. This means that only the diffusion coefficient D goes to zero as a result of the complete localization of the electronic states at the Fermi level. In the preceding sections, we have stressed that the amorphous V_xSi_{100-x} alloys enter an insulating regime, while the value of $N(E_F)$ is kept finite. It is our purpose in this section to examine how this situation is realized in the amorphous V_xSi_{100-x} alloy system.

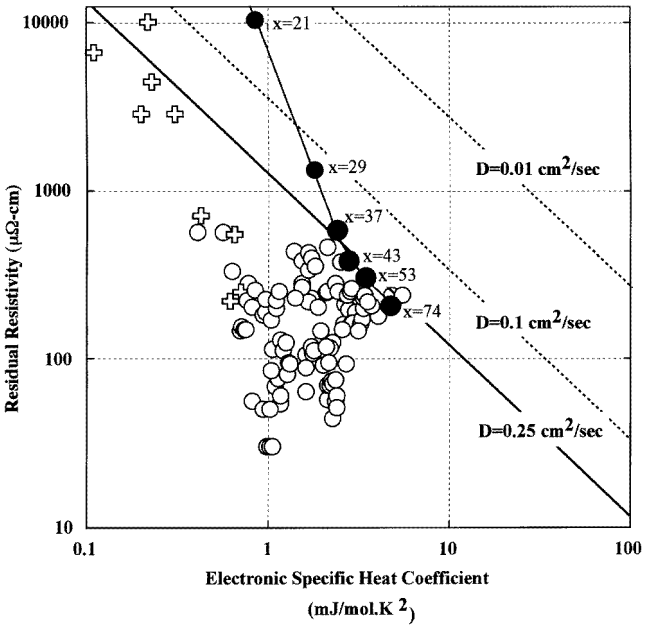

Figure 21. The residual resistivity plotted against the electronic specific heat coefficient for the amorphous V_xSi_{100-x} alloys (●) with $x = 21$, 29, 37, 43, 53, and 74, in the metallic regime, together with the data for a number of amorphous alloys (○) and quasicrystals (✣) [27]. Straight dotted lines represent constant-diffusion coefficient lines with $D = 0.1$ and 0.01 cm^2 s^{-1}. A 'high-resistivity limiting curve' with the diffusion coefficient $D = 0.25$ cm^2 s^{-1} is shown as a thick solid line.

The ρ_0–γ diagram is reproduced in figure 21 on a log–log scale for the large number of amorphous alloys and quasicrystals studied so far [28]. Here the high-resistivity limiting curve with $D = 0.25$ cm^2 s^{-1} is shown as a solid line. As mentioned above, one way of approaching the insulating regime is to reduce $N(E_F)$ to zero. This would accompany a diminishing D. In this case, the set of (ρ_0, γ) data would cross the high-resistivity limiting line only when $N(E_F)$ became very small. This behaviour is observed for icosahedral quasicrystals.

The value of ρ_0 can be obtained by extrapolating the ρ–T curve to 0 K for the present amorphous V_xSi_{100-x} alloys in the metallic regime ($x \geqslant 21$). The data points (ρ_0, γ) thus obtained are plotted in figure 21. As is clear from the argument above, the 21 at.% V sample is marginal to the metallic regime, and shows a residual resistivity of 10^4 $\mu\Omega$ cm or 100 Ω^{-1} cm^{-1} with the sizable γ-value of 0.98 mJ mol^{-1} K^{-2}. Obviously, the (ρ_0, γ) data for samples with the V concentrations $x = 21$ and $x = 29$ fall above the high-resistivity

limiting line with $D = 0.25$ cm^2 s^{-1}.

It is interesting to note that the 21 at.% V sample behaves as if the diffusion coefficient D is only of the order of 0.05 cm^2 s^{-1}. Its smallness can be realized when it is compared with the diffusion coefficient of 10^{-4} cm^2 s^{-1} for the carbon atom in α-iron at about 1400 °C [30]. Nevertheless, we pointed out that the conductivity for the 21 at.% V sample still obeys a square-root temperature dependence below about 25 K, consistently with the ordinary weak-localization theory coupled with the enhanced electron–electron interaction. Thus, this sample must be put in the metallic regime group. We consider the appearance of the data points for the samples with $x < 30$ above the high-resistivity limiting curve to be strongly related to the emergence of the magnetism discussed in section 3.5. The apparent possession of an extremely low D-value suggests that the electronic specific heat coefficient is enhanced by the magnetism. Further work along these lines is of particular interest.

In summary, the atomic structure of the amorphous V_xSi_{100-x} alloys is identified as having a tetrahedrally bonded Si network into which V atoms are randomly embedded, when the V concentration is below 10 at.%, and can be described as having a local structure similar to that of the VSi_2 intermetallic compound, when its concentration exceeds about 20 at.%. The metal–insulator transition in this system is found to occur in the range between 15 and 20 at.% V, where the two local atomic structures are competing with each other. It is also found that, even in the insulating regime below 10 at.% V, the density of states at the Fermi level is found to remain finite. The electronic states at the Fermi level are completely localized, and originate from the V 3d states hybridized with the neighbouring Si 3p electrons. We also revealed that the V 3d localized states accompany the Curie–Weiss-type magnetism.

Acknowledgments

The authors wish to express their thanks to Professor T Matsuda, Aichi University of Education, for assistance with the measurements of the temperature dependence of the conductivity for the V-poor amorphous alloys. They are also indebted to Dr T Koyano, now at Tsukuba University, for constructing the DC sputtering apparatus employed in this experiment. In the early stages of this work, studies of the atomic and electronic structures were conducted with the help of the graduate students H Ishihara and T Oguchi, at Nagoya University at the time, and we are grateful for their invaluable help. One of the authors (UM) is also very grateful to Professor S Maekawa, Nagoya University, for valuable discussions on the magnetism appearing in the insulating regime.

References

[1] Rosenbaum T F, Milligan R F, Paalanen M A, Thomas G A, Bhatt R N and Lin W 1983 *Phys. Rev.* B **27** 7509
[2] Mott N F and Kaveh M 1983 *Phil. Mag.* B **47** 577
[3] Dodson B W, McMillan W L, Mochel J M and Dynes R C 1981 *Phys. Rev. Lett.* **46** 46
[4] Nishida N, Furubayashi T, Yamaguchi M, Morigaki K and Ishimoto H 1985 *Solid State Electron.* **28** 81
[5] Hertel G, Bishop D J, Spencer E G, Rowell J M and Dynes R C 1983 *Phys. Rev. Lett.* **50** 743
[6] Möbius A, Vinzelberg H, Gladun G, Heinrich A, Elefant D, Schumann J and Zies G 1985 *J. Phys. C: Solid State Phys.* **18** 3337
[7] Elefant D, Gladun C, Heinrich A, Schumann J and Vinzelberg H 1991 *Phil. Mag.* B **64** 49
[8] Abkemeier K M, Adkins C J, Asal R and Davis E A 1992 *Phil. Mag.* B **65** 675
[9] Asal R, Baker S H, Gurman S J, Bayliss S C and Davis E A 1992 *J. Phys.: Condens. Matter* **4** 7169
[10] Tanaka K, Furui K and Yamada M 1995 *J. Phys. Soc. Japan* **64** 4790
[11] Wright T, Popescu B, Adkins C J and Davis E A 1996 *J. Phys.: Condens. Matter* **8** 6737

[12] Boghosian H H and Howson M A 1990 *Phys. Rev.* B **41** 7397
[13] Chui T, Deutscher G, Lindenfeld P and McLean W L 1981 *Phys. Rev.* B **23** 6172
[14] Wegner F J 1979 *Z. Phys.* B **35** 207
[15] Möbius A 1985 *J. Phys.: Solid State Phys.* **18** 4639
[16] Regan M J, Rice M, Fernandez van Raap M B and Bienenstock A 1994 *Phys. Rev. Lett.* **73** 1118
[17] Mael D, Yoshizumi S and Geballe T H 1986 *Phys. Rev.* B **34** 467
[18] Mott N F 1967 *Adv. Phys.* **16** 49
[19] Efros A L and Shklovskii B I 1975 *J. Phys. C: Solid State Phys.* **8** L49
[20] Reilly O J and Spear W E 1978 *Phil. Mag.* B **38** 295
[21] Fortner J and Lannin J S 1989 *Phys. Rev.* B **39** 5527
[22] Villars P and Calvert L D 1985 *Pearson's Handbook of Crystallographic Data for Intermetallic Phases* vol 1, ed P Villars and L D Calvert (Metals Park. OH: American Society of Metals)
[23] Zeller R C and Pohl R O 1971 *Phys. Rev.* B **4** 2029
[24] Lasjaunias J C, Laborde O and Gottlieb U 1993 *J. Low Temp. Phys.* **92** 335
[25] Mertig M, Pompe G and Hegenbarth E 1984 *Solid State Commun.* **49** 369
[26] Gottlieb U, Sulpice A, Madar R and Laborde O 1993 *J. Phys.: Condens. Matter* **5** 8755
[27] Tokura Y, Taguchi Y, Okada Y, Fujimori Y, Arima T, Kumagai K and Iye Y 1993 *Phys. Rev. Lett.* **70** 2126
[28] Mizutani U 1993 *Phys. Status Solidi* b **176** 9
[29] See, for example,
Mott N F 1990 *Metal–Insulator Transitions* (London: Taylor and Francis) p 33
[30] Kittel C 1996 *Introduction to Solid State Physics* 7th edn (New York: Wiley) p 544